Aerodynamic noise induced by laminar and turbulent boundary layers over rectangular cavities [*]

Xavier Gloerfelt[†] Christophe Bogey[‡] Christophe Bailly[§] and Daniel Juvé[¶]

Laboratoire de Mécanique des Fluides et d'Acoustique
Ecole Centrale de Lyon & UMR CNRS 5509
BP 163, 69131 Ecully cedex, France.

Abstract

The structure of an unsteady flow past a rectangular, open cavity is investigated using numerical simulations. Particular attention is drawn to the three-dimensional geometry effects, and to the turbulent state of the incoming boundary layer. The consequences on noise generation are studied. Two-dimensional DNS allows a reconstruction of the feedback loop giving rise to the self-sustained oscillations, but DNS is restricted to thick laminar upstream boundary layers. Cavity flows with higher Reynolds numbers are computed by 3-D Large Eddy Simulations, based on high order algorithms, by considering that the interactions of coherent structures with the downstream edge are predominant in such flows. The three-dimensional structure of the recirculating zone is illustrated and its influence on the shear layer dynamics is shown . In the same way as the incoming turbulence level, these modulations induce jittering of vortex-corner interactions, a decrease in feedback coherence, and thus a reduction of the radiated noise.

1. Introduction

Flow past an open cavity is known to give rise to self-sustained coherent oscillations of the impinging shear layer, as well as intense associated noise radiation. It has been studied by numerous investigators in the past because of its practical interest and because of the diversity of the theoretical questions involved. The self-sustained oscillations arise from a feedback loop consisting of the following chain of events : impingement of vortical perturbations on the downstream corner, generation of pressure disturbances (both acoustic and aerodynamic), influence from the impingement region on the receptive region of the shear layer located at the upstream corner, conversion of this influence into new fluctuations, amplification of the vortical perturbations with convection by the shear layer resulting in a new impingement, closing the loop.

This complex phenomenon is often greatly simplified to build lumped models such as the Rossiter formula[1] : the free shear layer is viewed as two-dimensional, and the recirculating flow is neglected. These approximations have provided insight into the principal oscillation frequencies. In this kind of semi-empirical model, a good deal of significance is attached to the highly localized vortices. However, experimental observations for fully turbulent cases have not always indicated their presence. Although, for the purpose of predicting the frequencies of discrete tones, the details of these physical processes may not be extremely crucial, their knowledge is of importance to noise suppression efforts.

The three-dimensional features of cavity flows have received relatively less attention. The streamwise vortices in the shear layer, side walls effects on the shear layer and in the cavity, or Taylor-Görtler type instabilities arising from the strong curvature of the recirculating flow can provide different sources of three-dimensionalities. The spanwise structure of the free shear layer along the mouth of a cavity has been visualized by Rockwell and Knisely[2] using the hydrogen bubble technique and reveals the interaction of secondary (longitudinal) and primary (Kelvin-Helmholtz) vorticity. The large-scale recirculation vortex between the shear layer and the walls of the cavity is felt to influence this three dimensionality. The existence of this zone can alter the average trajectory of the incident vortices, and may modulate the corresponding vortex-corner interaction. In the 2-D numerical study of Pereira and Sousa,[3] the modulations seem to occur at the upstream region of the separated layer due to recirculation unsteadiness. In the early experiments of Maull and East[4] and Kistler and Tan,[5] the flow inside the cavity is organized in cellular streamwise structures. The studies of driven-cavity flow[6] also indicate that the spanwise aspect ratio has a significant effect upon the mean eddy structure inside the cavity. Kuo and Huang[7] have investigated the effects of either

[†]Post-doc student

[‡]Research scientist, Member AIAA

[§]Assistant Professor, Member AIAA

[¶]Professor, Member AIAA

a positively or a negatively sloped bottom of the cavity, and show how the modified recirculating flow perturbs the unstable shear layer. The recirculation can also play an important role in the appearance of low-frequency modulations in the vortex-corner interaction patterns.[8]

The overall purpose of this study is to examine the three-dimensional features of the cavity flow, and to measure the influence of the recirculating flow on the mechanism producing self-sustained oscillations. Computational Aeroacoustics is used to probe these effects, and to provide detailed insight into the relation between vortex interaction and induced sound field. The first part of this paper describes the computational modelling for aeroacoustic simulations. In the second part, we present the two-dimensional direct computation of a rectangular cavity with a relatively thick incoming boundary layer. In the third part, the effects of the spanwise width on the oscillating flow are adressed. The repercussion of the laminar or turbulent state of the boundary layer inflow on the radiated sound-field is discussed in the last section.

2. Computational modelling

2.1 Governing equations

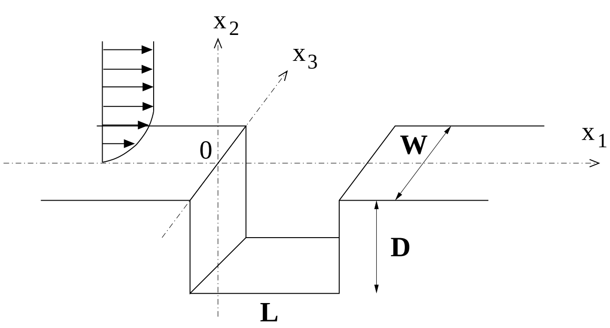

Figure 1: Sketch of the flow domain and coordinate system.

A schematic view of the flow domain is shown in figure 1. The origin of the coordinate system is located at the middle of the upstream corner. The governing equations are the unsteady compressible three-dimensional Navier-Stokes equations. They are expressed in a conservative form in the cartesian coordinate system of figure 1. In Large Eddy Simulation, only the large-scale structures are computed explicitely, and the small scales are modelled. The governing equations are obtained after spatial filtering, denoted by a bar. The velocity components are decomposed into a resolved part, $\widetilde{u_i} = \overline{\rho u_i}/\overline{\rho}$, using Favre averaging, and an unresolved part, u_i''. The resulting system solved in the present study is :

$$\frac{\partial \mathbf{U}}{\partial t} + \frac{\partial \mathbf{E_e}}{\partial x_1} + \frac{\partial \mathbf{F_e}}{\partial x_2} + \frac{\partial \mathbf{G_e}}{\partial x_3} - \frac{\partial \mathbf{E_v}}{\partial x_1} - \frac{\partial \mathbf{F_v}}{\partial x_2} - \frac{\partial \mathbf{G_v}}{\partial x_3} = 0 \quad (1)$$

where:

$$\begin{aligned}
\mathbf{U} &= (\overline{\rho}, \overline{\rho}\widetilde{u_1}, \overline{\rho}\widetilde{u_2}, \overline{\rho}\widetilde{u_3}, \overline{\rho}\widetilde{e})^t \\
\mathbf{E_e} &= (\overline{\rho}\widetilde{u_1}, \widetilde{p} + \overline{\rho}\widetilde{u_1}^2, \overline{\rho}\widetilde{u_1}\widetilde{u_2}, \overline{\rho}\widetilde{u_1}\widetilde{u_3}, (\overline{\rho}\widetilde{e} + \widetilde{p})\widetilde{u_1})^t \\
\mathbf{F_e} &= (\overline{\rho}\widetilde{u_2}, \overline{\rho}\widetilde{u_2}\widetilde{u_1}, \widetilde{p} + \overline{\rho}\widetilde{u_2}^2, \overline{\rho}\widetilde{u_2}\widetilde{u_3}, (\overline{\rho}\widetilde{e} + \widetilde{p})\widetilde{u_2})^t \\
\mathbf{G_e} &= (\overline{\rho}\widetilde{u_3}, \overline{\rho}\widetilde{u_3}\widetilde{u_1}, \overline{\rho}\widetilde{u_3}\widetilde{u_2}, \widetilde{p} + \overline{\rho}\widetilde{u_3}^2, (\overline{\rho}\widetilde{e} + \widetilde{p})\widetilde{u_3})^t \\
\mathbf{E_v} &= (0, \widetilde{\tau_{11}} + \mathcal{T}_{11}, \widetilde{\tau_{12}} + \mathcal{T}_{12}, \widetilde{\tau_{13}} + \mathcal{T}_{13}, \\
&\qquad \widetilde{u_i}(\widetilde{\tau_{1i}} + \mathcal{T}_{1i}) - \widetilde{q_1} - c_v \mathcal{Q}_1)^t \\
\mathbf{F_v} &= (0, \widetilde{\tau_{21}} + \mathcal{T}_{21}, \widetilde{\tau_{22}} + \mathcal{T}_{22}, \widetilde{\tau_{23}} + \mathcal{T}_{23}, \\
&\qquad \widetilde{u_i}(\widetilde{\tau_{2i}} + \mathcal{T}_{2i}) - \widetilde{q_2} - c_v \mathcal{Q}_2)^t \\
\mathbf{G_v} &= (0, \widetilde{\tau_{31}} + \mathcal{T}_{31}, \widetilde{\tau_{32}} + \mathcal{T}_{32}, \widetilde{\tau_{33}} + \mathcal{T}_{33}, \\
&\qquad \widetilde{u_i}(\widetilde{\tau_{3i}} + \mathcal{T}_{3i}) - \widetilde{q_3} - c_v \mathcal{Q}_3)^t
\end{aligned}$$

where c_v is the specific heat at constant volume. The quantities $\overline{\rho}$, $\widetilde{p}$, $\widetilde{u_i}$ are the density, pressure, and velocity components. For a perfect gas, the total energy per mass unit $\widetilde{e}$ is :

$$\widetilde{e} = \widetilde{p}/[(\gamma - 1)\overline{\rho}] + (\widetilde{u_1}^2 + \widetilde{u_2}^2 + \widetilde{u_3}^2)/2, \quad \text{and} \quad \widetilde{p} = r\overline{\rho}\widetilde{T},$$

where $\widetilde{T}$ is the temperature, r the gas constant, and γ the ratio of specific heats. The viscous stress tensor $\widetilde{\tau_{ij}}$ is modelled as a Newtonian fluid $\widetilde{\tau_{ij}} = 2\mu\widetilde{S_{ij}}$, where μ is the dynamic molecular viscosity, and $\widetilde{S_{ij}}$ the deviatoric part of the resolved deformation stress tensor :

$$\widetilde{S_{ij}} = \frac{1}{2}\left(\frac{\partial \widetilde{u_i}}{\partial x_j} + \frac{\partial \widetilde{u_j}}{\partial x_i} - \frac{2}{3}\delta_{ij}\frac{\partial \widetilde{u_k}}{\partial x_k}\right)$$

The heat flux component $\widetilde{q_i}$ models thermal conduction in the flow with Fourier's law $\widetilde{q_i} = -(\mu c_p/\sigma)(\partial\widetilde{T}/\partial x_i)$, where σ is the Prandtl number, and c_p the specific heat at constant pressure.

The effects of the fine scales are present in system (1) through the subgrid scale stress tensor $\mathcal{T}_{ij}$ and the subgrid scale heat flux $\mathcal{Q}_i$. We use the simple closure model of Smagorinsky, with $C_S = 0.18$. In presence of solid walls, an empirical law has to be introduced to describe the scale reduction that occurs near the walls. This is implemented via a simple exponential van Driest damping.

The Smagorinsky model is only used for the fully turbulent simulation, and no model is applied for the initially laminar cases because it cannot describe the turbulent transition. Nevertheless, the moderate value taken by the turbulent viscosity μ_t in the computations and the combination of a fine grid resolution with high order algorithms allows the description of the small scales up to the grid cut-off wave number.

2.2 Algorithm and boundary conditions

Algorithm

The governing equations (1) are integrated in time using an explicit low-storage six-step Runge-Kutta scheme, optimized in the wave number space, for the convective terms. Because of their slower time evolution, the viscous terms are integrated in the last substep without affecting the global accuracy. The gradients are solved on the rectangular nonuniform grid by using optimized finite difference coefficients for an eleven-point stencil for the convective fluxes, and 4^{th} order finite differences for the viscous and heat fluxes. As part of the algorithm, a selective damping term built on an eleven-point stencil is incorporated in each direction to eliminate numerical oscillations originating from regions with large gradients and/or from the boundary treatment. The coefficients of the Runge-Kutta, of the finite differences and of the damping schemes are given in Bogey and Bailly.[9]

Solid walls

On all solid boundaries, the no-slip conditions $u_1 = u_2 = u_3 = 0$ are imposed, with $\partial p/\partial n = 0$, where n is the direction normal to the rigid surface. The wall temperature is calculated by using the adiabatic condition. For the sharp corners formed by the intersection of planar cavity surfaces, the variables are determined by using the interior scheme, thereby avoiding any ambiguity regarding the normal direction.

Radiation conditions

At the upstream and upper boundaries, the radiation boundary conditions of Tam and Dong,[10] using a far-field solution of the linearized Euler equations, are applied. At the outflow, we combine the outflow boundary conditions of Tam and Dong, where the far-field solution is modified to allow the exit of vortical and entropic disturbances, with a sponge zone to dissipate vortical structures. This sponge zone uses grid stretching and a progressively applied Laplacian filter.

Lateral boundaries

The treatment of the lateral boundaries raises serious problems for an aeroacoustic simulation. The most common choice in CFD calculations is the use of either periodic, symmetric conditions, or slip walls. They are precluded for an acoustic calculation because they reflect acoustic waves. Therefore we modelize the two sidewalls like other rigid wall conditions. The lateral boundaries above the cavity are then free boundaries, where the non-reflecting condition combined with a sponge zone is used.

Method of generating inflow turbulence

To create the unsteady, stochastic inflow condition for spatial turbulent simulations, we use Random Fourier Modes (RFM), following the construction of the SNGR model.[11] The turbulent inlet field is generated by the sum of N independent RFM, with amplitudes $\hat{u}_n$ determined from the turbulent kinetic energy spectrum. The fluctuating velocity field is then expressed as a Fourier series :

$$\mathbf{u}'(\mathbf{x}, t) = \sum_{n=1}^{N} \hat{u}_n \cos(\mathbf{k}_n.(\mathbf{x} - \widetilde{\mathbf{u}_0} t) + \omega_n t + \psi_n)\mathbf{a}_n$$

where ψ_n, $\mathbf{k}_n$, $\mathbf{a}_n$ are random variables with given probability density functions. An unfrozen turbulent field is obtained by incorporating the convection velocity $\widetilde{\mathbf{u}_0}$ and the pulsation ω_n, accounting for the temporal evolution of the perturbations. In the present turbulent simulation, we have taken $N = 200$ RFM and ω_n is deduced from the Heisenberg time, $\omega_n = 2\pi u' k_n$. This stochastic velocity field is multiplied by the vertical profiles of *rms* velocities from Spalart's[12] temporal DNS at $\mathrm{Re}_{\delta_\theta} = 1410$. This procedure gives the correct vertical distributions but has two drawbacks. First, the incompressibility condition is no longer ensured and the excitation becomes noisy. This spurious radiation is however sufficiently weak compared to cavity noise. Second, it cannot provide the phase relationship between individual Fourier modes, and turbulence decays downstream of the inlet plane until the near wall cycle of turbulence production has been established. Nevertheless, the temporal evolution through Heisenberg's time allows a very quick by-pass transition to turbulence.

2.3 Simulation parameters

Flow configurations

The five simulations performed are summarized in tables 1 and 2. For the initially laminar inflow configurations, $u_{1_0}(x_2)$ corresponds to a third order polynomial expression of the Blasius profile, and no forcing is applied. For the initially turbulent simulation, the mean profile at the inlet is obtained from Spalart's temporal boundary layer simulation at $\mathrm{Re}_{\delta_\theta} = 1410$, to which inflow turbulence, generated by the method described in §2.2, is superimposed. The freestream air temperature is T_∞, and the static pressure p_∞ is taken as 1 atm.

Run	Aspect ratio L/D	Aspect ratio L/W	Régime	Model
2Dr2TH	2	-	lam.	DNS
3Dr1N	1	1.28	lam.	no model
3Dr1W	1	0.5	lam.	no model
3Dr3L	3	0.78	lam.	no model
3Dr3T	3	0.78	turb.	SM

Table 1: Recapitulative table of the simulations presented. The simulation names are built as follows : dimension (2D or 3D) - longitudinal aspect ratio (r..) - main characteristic (TH : thick, L : laminar or T : turbulent upstream boundary layer, N : narrow or W : wide spanwise dimension W). SM = Smagorinsky model.

Numerical specifications

The computational mesh is nonuniform and cartesian, refined near the walls. The number of grid points in each direction and the size of the computational domain are given in table 3. For explicit time marching schemes, the time step must satisfy the CFL stability criterion. For the turbulent run 3Dr3T, $\Delta t = 1. \times \Delta x_{2_{min}}/c_\infty = 5.8 \times 10^{-8}$ s, and a large number of time iterations are needed. The 2-D computation lasts 4 hours on a Nec

Run	Mach	Re_D	$Re_{\delta_{\theta_R}}$	H	T_∞
2Dr2TH	0.7	41000	1664	2.6	298.15
3Dr1N	0.6	28700	270	2.2	320.26
3Dr1W	0.6	28700	270	2.2	320.26
3Dr3L	0.8	48600	990	2.3	320.26
3Dr3T	0.8	48600	2250	1.9	320.26

Table 2: Flow parameters. H is the shape factor, $H = \delta_{\theta_R}/\delta^*_R$. The thicknesses (suffix R) are evaluated at the upstream edge of the cavity when the mean flow is converged.

SX-5. Runs 3Dr1N and 3Dr1W require 11 and 14 hours respectively. The two other 3-D computations 3Dr3L and 3Dr3T last 40 hours for 5.4 million grid-points (CPU time of 0.6 μs per grid point and per iteration). These latter simulations match two configurations of Karamcheti's experiments.[13]

Run	$N_1; N_2; N_3$ cavity	$N_1; N_2; N_3$ outside	$\frac{L_1}{D}; \frac{L_2}{D}; \frac{L_3}{D}$
2Dr2TH	147;161;-	501;440;-	12;8.5;-
3Dr1N	41;33;41	121;132;71	5.8;3.1;1.4
3Dr1W	41;33;81	121;132;109	5.8;3.1;2.7
3Dr3L	87;71;123	235;130;151	12.8;7.8;5.2
3Dr3T	87;71;123	235;130;151	12.8;7.8;5.2

Table 3: Numerical parameters.

3. Bidimensional simulation of thick upstream boundary layer

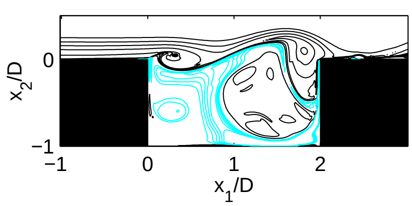

Figure 2: Snapshot of vorticity contours (16 contours between $\omega D/U_\infty = -10.5$ and 1.36: (——) negative contours, (——) positive contours).

We start with run 2Dr2TH ($L/D = 2$, M=0.7), where the incoming boundary layer is relatively thick ($L/\delta_{\theta_R} \simeq 50$). Figure 2 shows a snapshot of isovorticity contours : Kelvin-Helmholtz eddies are shed from the leading edge separation. Substantial severing is observed as they impinge the downstream edge. The lower portion of the impinging vortex is swept downwards along the downstream vertical face of the cavity, and flow separation from the wall is rapidly induced, producing vorticity of opposite sign. In the 2-D simulations, this vorticity wraps around the clockwise-rotating large-scale recirculation, arising from the clipped part of the incident vortices. It is first confined between the walls and the main recirculation, producing a reverse wall jet on the front face and on the bottom of the cavity. This wall jet induces a counter-rotating recirculation zone in the upstream half of the cavity. The two principal recirculations are clearly distinguishable in the streamline patterns of figure 3.

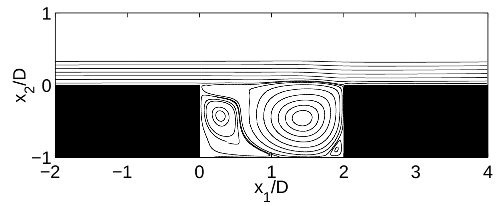

Figure 3: Streamlines of the mean flow 2Dr2TH.

The mean velocity profiles $u_{0_1}(x_2)$ change from a boundary layer profile to a shear layer profile with a weak rate of widening of the momentum thickness, $d\delta_\theta/dx_1 \simeq 0.006$. The same value is reported in Sarohia[14] measurements for a $L/\delta_{\theta_R} = 52.5$ configuration. In the cavity, there are marked discrepancies between measured and computed mean profiles. Given the two-dimensional nature of the simulation, the cause seems to be that the flow in the cavity is turbulent.

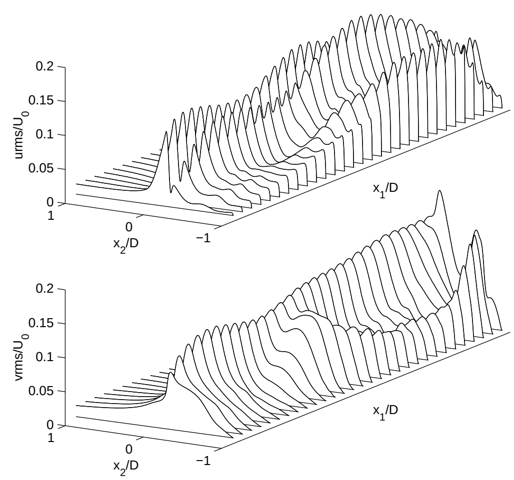

Figure 4: Longitudinal velocity fluctuations u_{rms} (top), and vertical velocity fluctuations v_{rms} (bottom) for the 2Dr2TH run. Profiles made every $L/30$ between $x_1 = 0$ and $x_1 = L$.

The intensity of fluctuations, defined as :

$$u_{rms} = \frac{\sqrt{< u_1'^2 >}}{U_\infty} \qquad v_{rms} = \frac{\sqrt{< u_2'^2 >}}{U_\infty}$$

where <> denote the time average, are plotted in figure 4. The u_{rms} profiles rapidly show the appearance of a double peak. For forced shear layers,[15] or for cavities with a large ratio L/δ_θ,[16] the double peak appears progressively. The profiles are considerably affected by the high levels taken by the recirculating flow. The maximum amplitude $u_{rms} = 0.16$ is coherent with previous experimental results of Sarohia[14] for laminar flow. The vertical velocity fluctuations show a bell-shaped distribution all along the shear layer with the same order of intensity as the horizontal ones, $v_{rms} = 0.14$. The experiments of Oster and Wygnanski,[15] for forced mixing layers, underline a reinforcement of the vertical component and a decrease of intensities in the spanwise direction, in comparison with the unperturbed flow. This suggests a bidimensionalisation of the flow, which can explain why the vertical intensities are not overestimated in the 2-D simulations.

The Strouhal number based on the momentum thickness is $\mathrm{St}_\theta = 0.014$, near the value 0.017 for the most unstable frequency of a hyperbolic-tangent velocity profile in the linear stability analysis. The initial vortex-formation frequency f_r is seen to match the forcing frequency f_0. The level of the fundamental f_0 suppresses the growth of the subharmonic $f_0/2$, and vortex pairings are delayed. A row of well-aligned vortices is generated and interacts with the downstream edge. The absence of pairing events is in accordance with the weak growth rate of the shear layer. The acoustic results are presented in an earlier paper,[17] and indicate that the acoustic emission is directly linked to the impingement process.

Even if the global behaviour conforms to measurements in this configuration with a relatively thick incoming boundary layer, some limitations inherent to the bidimensional approach are noticeable. The fact that the vorticity of opposite sign arising from the corner interaction surrounds the principal recirculation produces an inverse cascade of energy toward this large-scale eddy. This phenomenon becomes critical when the incident boundary layer is thin ($L/\delta_{\theta_R} > 70$). The large recirculating eddy can detach from the cavity bottom under the influence of the counter-rotating vortex. This pair of vortices is then violently ejected, overshadowing the role of the smaller eddies of the shear layer. This new régime is sometimes called the wake mode[18] because of the drag increase. Vortex stretching, necessarily 3-D, significantly modifies the mixing between the clipped part of the shear layer and the induced counter-rotating vortex, and prevents untimely transition to the wake mode.[19]

4. Effect of the width on cavity flow and its radiated field

4.1 Topology of flow structures

We now deal with the 3-D simulations 3Dr1N and 3Dr1W, where solely the width W is varied. Figures 5 and 6 show perspective views of the Q-criterion. The vorticity field for the 3Dr1N computation, depicted in figure 5, displays a typical view of cavity flow. Coherent

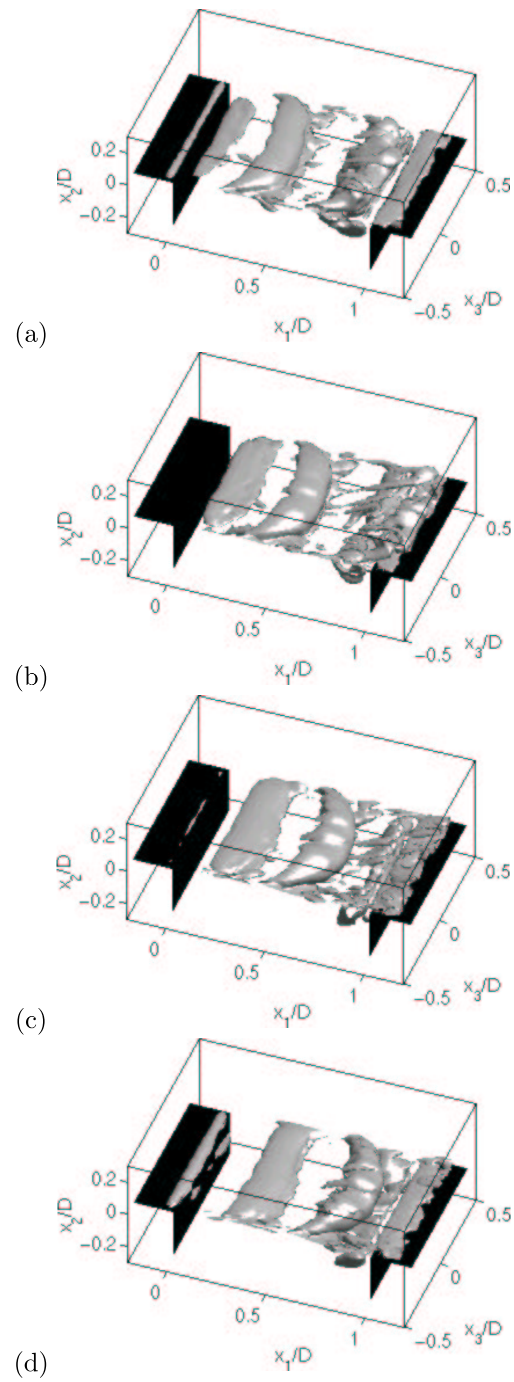

Figure 5: Run 3Dr1N; Perspective views of the Q-criterion at four instants during one cycle of oscillations, $T = 1/f_4$ (mode $n = 3$).

spanwise rolls are convected downstream. The vortex-formation frequency f_r corresponds to the f_3 component noted hereafter. The influence of the end walls is visible and induces a stretching of the primary vortices, producing a warping of the axis of the primary vortices across the entire flow. Moreover, streamwise vorticity can be seen in the mature evolution between two adjacent rolls, and is associated to a Taylor-Görtler instability. The core of a primary structure just before impingement (the last roll in figure 5 (a) for example) becomes increasingly three dimensional and severe distorsion is visible as it impinges in figure 5 (b). These observations are conform to the top views of Rockwell and Knisely[2] for a low-speed cavity flow in water. The complexity of the possible interaction patterns between the streamwise and spanwise vorticities, and different forms of pairing events are addressed in recent 3-D spatial simulations of mixing layers.[20]

In the wide cavity case (figure 6), a quasi-two-dimensional pairing (localized just upstream of the front wall) is distinguishable. A Kelvin-Helmholtz roll is slowed when it arrives on the impingement corner, and the preceding vortex is caught in its strain field. They begin to rotate around each other in figure 6 (b). Their interaction takes the form of a braid of two merging entwisted vortices in figure 6 (c), which resembles the helical pairing as defined by Chandrsuda *et al.*[21] This new double-sized vortex is immediately clipped into two parts in the impingement process; one part is directed downwards in the cavity, and the other is evacuated in the reattached boundary layer. Thinner streamwise vortices (with, in fact, an inclinaison of 45°) are generated in the regions between two rolls, from the large curvature of the trail of the vortices. Other less coherent streamwise vorticity can be identified in the lower part of the shear layer, and originates from the interface with the recirculation zone. This vorticity perturbs the rolling-up of the new vortices at the upstream corner. The new roll in figure 6 (a)(b) originating from the leading edge is very distorted and elongated in the streamwise direction. The next one, shedded in figure 6 (c) is more two-dimensional but is also severely elongated. The two vortices begin to interact in figure 6 (d) in a process close to a tearing event, induced by the recirculating flow.

4.2 Turbulence intensities

The fluctuation levels for the simulations 3Dr1N and 3Dr1W are higher than those of the 2-D thick configuration. The double peak distribution, characteristic of the presence of well-aligned vortices in the thick shear layer, are now replaced by a narrow peak at the location of the shear layer, which enlarges further downstream (figure 7). The jittering effect has smeared the peaks into a single-peak profile. The random merging visible on vorticity snapshots also explains this single peak. The most striking result is the considerable reduction of the fluctuations inside the cavity. This can be explained by the deeper aspect ratio, and the thinner incoming bound-

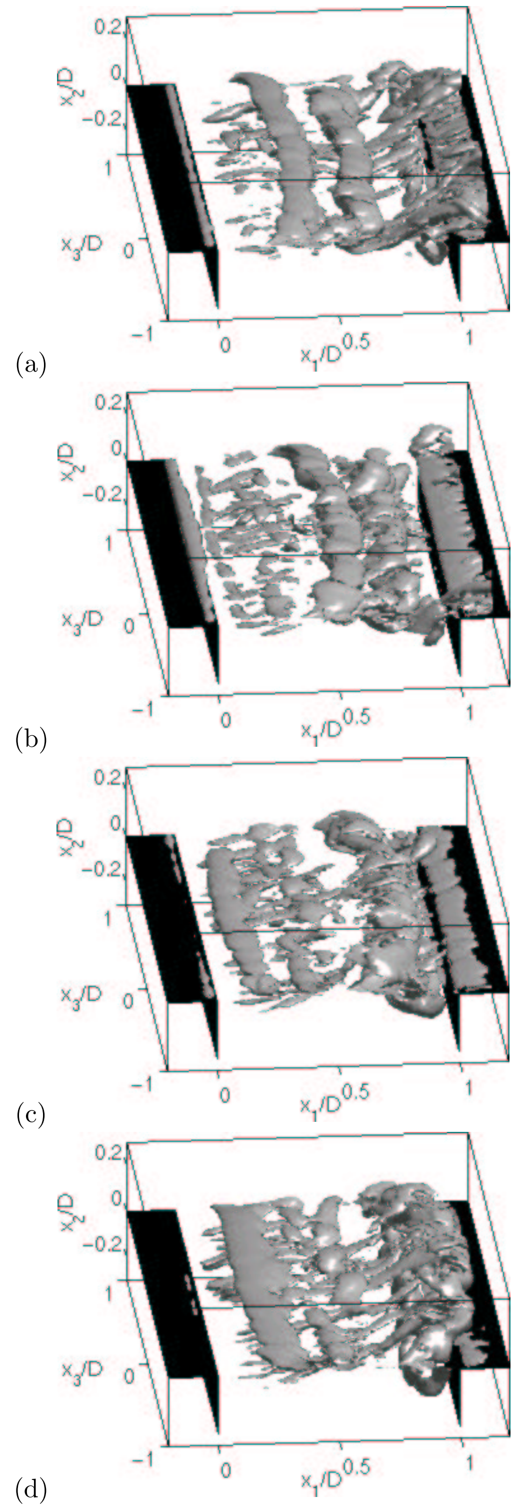

Figure 6: Run 3Dr1W; Perspective views of the Q-criterion at four instants during one cycle of oscillations, $T = 1/f_3$ (mode $n = 2.5$).

ary layer relatively to the depth ($D/\delta_\theta \simeq 110$ versus 25 in the 2Dr2TH simulation). The size of the clipped portions of vortices swept in the cavity is then strongly reduced. Moreover, the inspection of the flow inside the cavity does not reveal a well-defined recirculation eddy but rather a turbulent mixing and a cascade of energy towards smaller scales.

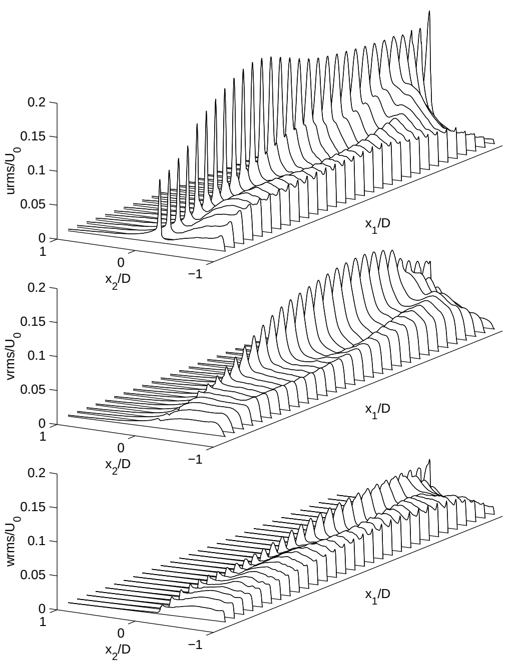

Figure 7: *Rms* fluctuating velocity statistics for 3Dr1N simulation. Profiles made every $L/30$ between $x_1 = 0$ and $x_1 = L$.

Only the longitudinal evolutions for the narrow case 3Dr1N have been reproduced in figure 7 because the shape of fluctuating velocities for the wider cavity flow shows exactly the same characteristics. A quantitative comparison is provided in figure 8, and the maxima of each velocity component are reported in table 4. u_{rms} and v_{rms} have similar amplitudes around 20% of the freestream velocity, which is in good agreement with the measurements of Forestier[16] for a $L/D = 0.58$ cavity at M=0.8. The levels are slightly higher for the 3Dr1W case, because of the stronger coherence of the oscillations. The spanwise fluctuation levels are considerably weaker, around 9%, showing a clear bidimensionalisation of the flow like in the Oster and Wygnanski[15] experimental study.

Velocity fluctuations spectra along the shear layer show the coexistence of several tonal components. The five principal values of the frequencies are given in the dimensionless form of Strouhal numbers, St$= fL/U_\infty$, in table 5. They compare well with those obtained with Rossiter's formula[1] for both cases, and can then be considered as the admissible frequencies : each feedback-

	u_{rms}	v_{rms}	w_{rms}	$d\delta_\theta/dx_1$
2Dr2TH	0.16	0.14	-	0.006
3Dr1N	0.20	0.18	0.09	0.04
3Dr1W	0.22	0.22	0.09	0.04
3Dr3L	0.35	0.30	0.28	0.03
3Dr3T	0.27	0.25	0.26	0.03
Forestier[16]	0.23	0.23	-	0.035-0.07
Oster & Wygnanski[15]	0.21	0.3	-	0.02

Table 4: Maximal values of *rms* velocity fluctuations and estimation of spreading rates.

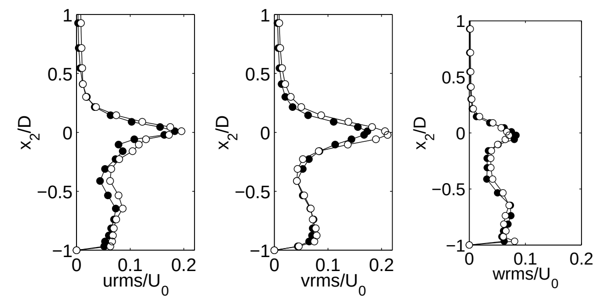

Figure 8: Comparison of *rms* velocity profiles at the location $x_1 = 2L/3$ for the 3Dr1N (-•-) and 3Dr1W (-○-) simulations.

tone satisfies a given phase difference over length L.

In order to investigate the streamwise evolution of the periodic components, velocity fluctuations have been recorded along the shear layer, every $L/20$ on the line joining the two corners of the cavity. The spectra are calculated over around ten cycles of the lower frequency f_1, and are averaged over 7 spanwise locations. The peak of each component at a given streamwise station, designated as $(u_{rms})_{M_i}$, is depicted in figure 9 for the narrow cavity and in figure 10 for the wide one. In the narrow case, the streamwise fluctuations are dominated by the first frequency f_1, which peaks near $x_1/L = 0.3$. The second predominant frequency is f_2, showing two longitudinal maxima. The vertical velocity indicates the coexistence of the five frequencies, which develop linearly, saturate further downstream at $x_1/L \simeq 0.7$, and then sink. The f_5 frequency reaches a first peak near $x_1/L = 0.5$. f_1 follows the the shape for the corresponding evolution of u_{rms} with a considerably lower amplitude (3% versus 14%). The spanwise velocity (not represented) is also characterized by a multiple frequency content but the levels are weaker, around 1%. The streamwise spectral component development for the wide case is radically different. The feature they share is the presence of several simultaneous tones, close to those of the narrower case (see table 5). The main difference is the greater emergence of the third frequency f_3 in the three velocity components. In the streamwise fluctuating velocity plot (figure 10), f_3 dominates, and peaks at $x_1/L = 0.6$,

	St_1	St_2	St_3	St_4	St_5
3Dr1N	**0.32**	0.66	**0.93**	**1.25**	1.55
3Dr1W	0.34	0.52	**0.85**	1.19	1.71
Rossiter	0.32	0.74	0.95	1.17	1.59
	$(n=1)$	$(n=2)$	$(n=2.5)$	$(n=3)$	$(n=4)$

Table 5: First five cavity tones calculated (the stronger peaks are in bold), compared with the results of Rossiter's formula.[1]

where the pairing event previously described for this configuration takes place. The vertical velocity spectra are also dominated by the third tone which shows a high amplitude comparable with u_{rms}, about 15%. The levels of the spanwise components are as weak as the narrow cavity flow, but indicate a pronounced f_3 frequency.

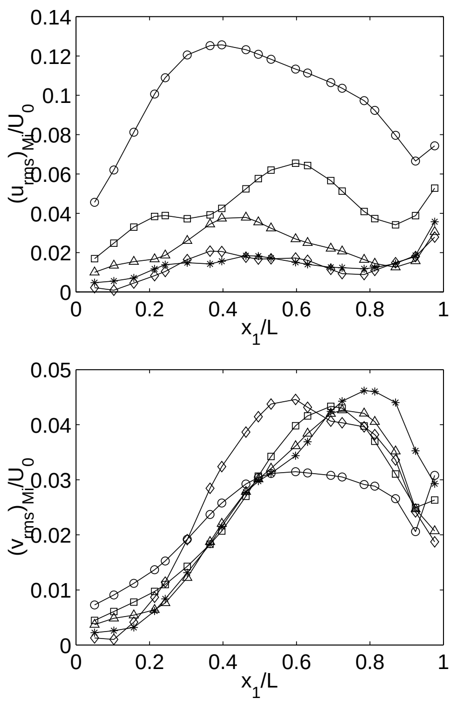

Figure 9: Streamwise evolution of spectral peaks along the line $x_2 = 0$ for the 3Dr1N run : ◦, St_1; □, St_2; Δ, St_3; ∗, St_4; ◇, St_5.

The low frequency component f_1 described for the 3Dr1N simulation is attributable to modulations of the vortex-corner interaction by the large-scale (i.e. low frequency) recirculating flow inside the cavity. Long-time examination suggests the likelihood of cycling between the patterns of interaction, like in Rockwell and Knisely experiments.[22] This low-frequency component is not a direct consequence of coalescence of adjacent vortices, but can be associated with the first phases of the vortex-vortex interaction leading to coalescence. The presence of the edge precludes the mature phases of pairing. In the wide cavity simulation 3Dr1W, the recirculation zone is more steady because the end-walls effects are reduced, which favours a well-defined interaction pattern. The flow is quasi-two-dimensional, and dominated by the third frequency f_3. The self-selection process of the feedback frequency is optimized with an early pairing event just upstream of the impingement corner. These results illustrate that, in addition to the feedback effect, the upstream moving part of the recirculation flow plays an important role in changing the oscillation characteristics of the shear layer.

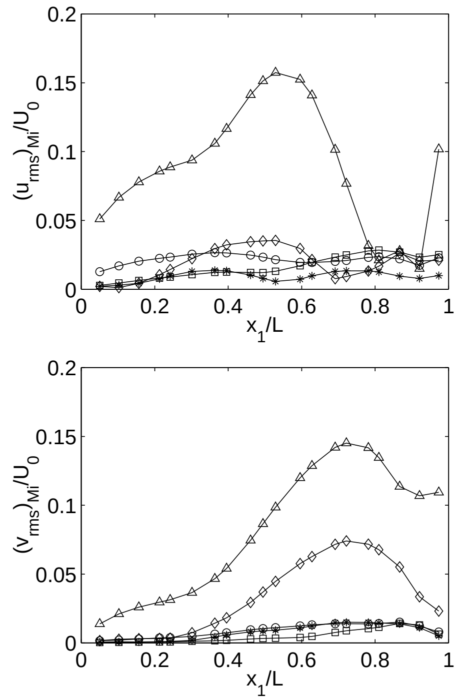

Figure 10: Streamwise evolution of spectral peaks along the line $x_2 = 0$ for the 3Dr1W run : ◦, St_1; □, St_2; Δ, St_3; ∗, St_4; ◇, St_5.

4.4 Acoustic field

The spectra of figure 11 show that the first three peaks have the same value for the two computations; they correspond to the dominant frequencies f_1, f_3 and f_4 in the velocity spectra (in bold in table 5). However, their respective amplitudes are different : f_1 and f_4 are predominant for the narrow case, whereas the wider one indicates a pronounced f_3 component. In this case, several harmonics are noticeable arising from the nonlinear distorsion. The frequency jump is clearly identifiable on the pressure fields of figure 12.

The spectra of figure 11 show a reduction in terms of sound pressure level over the entire spectra as a result of the smaller cavity width. A reduction of 15 dB is observed from the quasi 2-D (3Dr1W run, $L/W = 0.5$) to the 3-D (3Dr1N run, $L/W = 1.28$) configurations. The reduction in levels is present at all recording locations. These results conform to the measurements of Mendoza

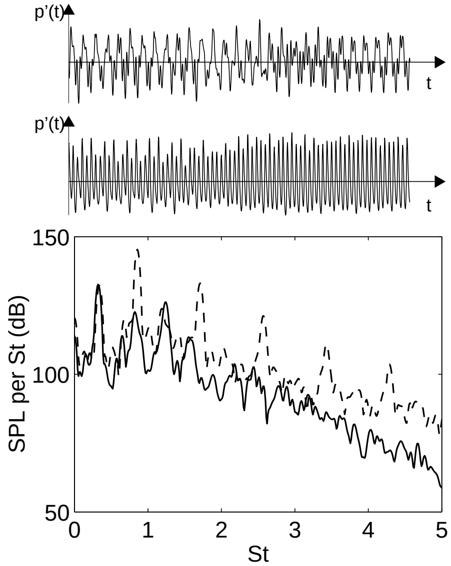

Figure 11: From top to bottom, pressure histories versus time for the 3Dr1N and 3Dr1W runs, and comparison of spectra of pressure fluctuations at $x_1/D = -0.97$ and $x_2/D = 1.46$ versus the Strouhal number : (——), 3Dr1N run and (— — —), 3Dr1W run.

and Ahuja,[23] and indicate that the spanwise coherence of the feedback-instability wave is lower for the narrow cavity ($L/W > 1$) than for the wider one ($L/W < 1$). The loss of coherence is produced by the unsteadiness of the recirculating flow in the narrower cavity.

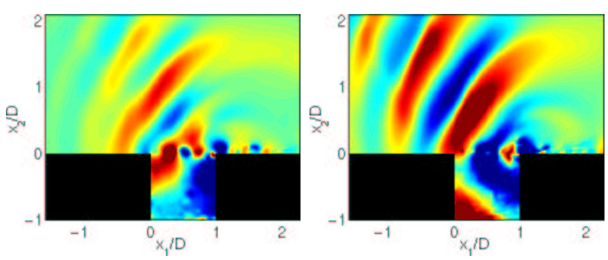

Figure 12: Pressure fields for the run 3Dr1N (on the left), and run 3Dr1W (on the right). Levels between -2000 and 2000 Pa.

5. Laminar and turbulent boundary layers ahead of a $L/D = 3$ cavity

5.1 Vorticity field

As shown by the snapshots of vorticity of figures 13 and 14, a large-scale vortex emerges from the turbulent background. This vortex is actually made up of a number of small-scales vortices. The centers of the coherent structures for the turbulent inflow are below those found for the laminar inflow, in agreement with the observations of Demetz and Farabee.[24] A further study of the flow structures indicates that the clusters of small scales are clipped as they impinge on the corner and travel down along the vertical surface, then upstream along the cavity floor, resulting in a wall jet-like flow.[25]

The interaction between streamwise vorticity and primary spanwise rolls enhances the mixing, and was postulated as the basis of the energy cascade towards smaller scales. Mushroom-shaped ejections are exhibited in the cross section of figure 14, as in the visualizations of Bernal and Roshko.[26] This is characteristic of streamwise vortices. Their tendency to move away in the radial direction is associated with curvature of the streamwise vortices imposed by the primary spanwise rolls.

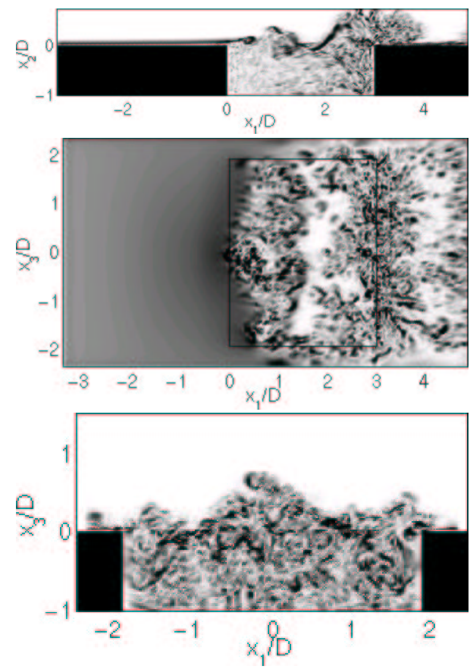

Figure 13: Snapshot of vorticity modulus $\|\boldsymbol{\omega}\|$ in run 3Dr3L. From top to bottom, side view at $x_3 = 0$, top view at $x_2 = 0.06D$, and cross section at $x_1 = 3.9D$.

5.2 Turbulence intensities

Rms fluctuating velocity profiles are given in figure 15 for the initially laminar case. The single peak distributions are similar to those found in figure 7, but they are enlarged by the randomness of small-scales. They can even encompass all the cavity depth further downstream, illustrating the relationship between the shear layer and the recirculating flow within the cavity. Their amplitude is greatly enhanced (about 30 %), and the most striking change concerns the development of the spanwise fluctuations, which reach the same amplitude as the two other components. The cavity flow is now highly turbulent and three dimensional. The comparison of the laminar and turbulent simulations in figure 16 reveals that the levels are slightly higher for the laminar case (see maximum values in table 4). In this case the in-

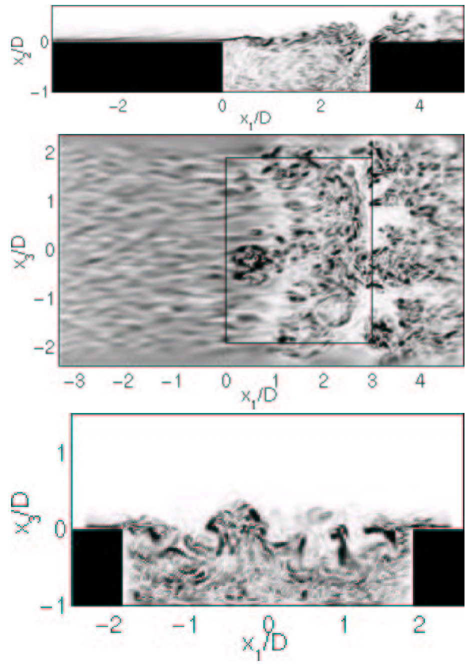

Figure 14: Snapshot of vorticity modulus $\|\boldsymbol{\omega}\|$ in run 3Dr3T. From top to bottom, side view at $x_3 = 0$, top view at $x_2 = 0.06D$, and cross section at $x_1 = 3.9D$.

tensity of u_{rms} reaches a maximum soon after the leading edge. It eventually stabilizes further downstream around an asymptotic value due to small-scale transition. The intensity of the fluctuation peak for the turbulent incoming boundary layer relaxes monotonically to approximately the same value as in the laminar boundary-layer case, but there is no overshoot.

5.3 Collective interaction

Figure 17 displays the early development of the shear layer. The initial shedding frequency is around $\mathrm{St}_\theta = 0.017$, which is close to the most unstable frequency predicted by the linear theory of stability. Further downstream the flow contains larger structures (i.e. lower frequency components). This frequency drop is associated with the successive or simultaneous coalescence of a number of vortices, referred to as collective interaction by Ho et Nosseir.[27] The low-frequency component (due to the upstream acoustic waves) forces the shear layer to undulate, and the vortices, shedded at the initial instability frequency, are displaced laterally. Owing to their induced field, the vortices are drawn together and coalesce into a large vortex (see figure 17). The passage frequency of the resulting coherent structure is then equal to the forcing frequency. This phenomenon participates in the selection of a single frequency, characteristic of flow with self-sustained oscillations. The necessary condition for this interaction is a high-amplitude low-frequency excitation, provided here by the intense acoustic field. The two principal consequences are the

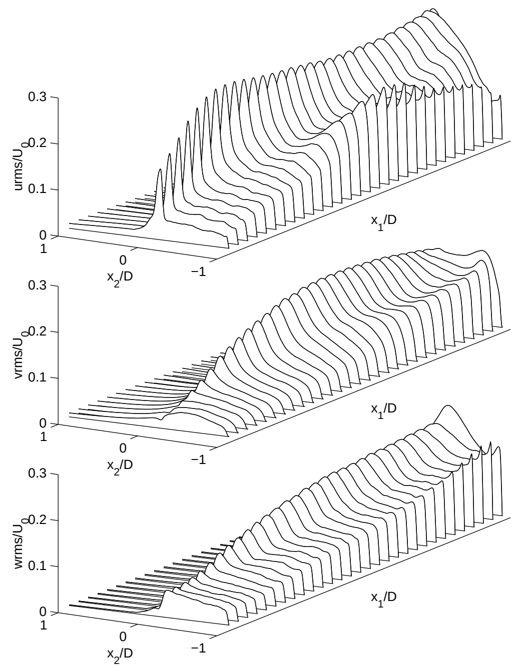

Figure 15: *Rms* fluctuating velocities statistics for 3Dr3L simulation. Profiles made every $L/30$ between $x_1 = 0$ and $x_1 = L$.

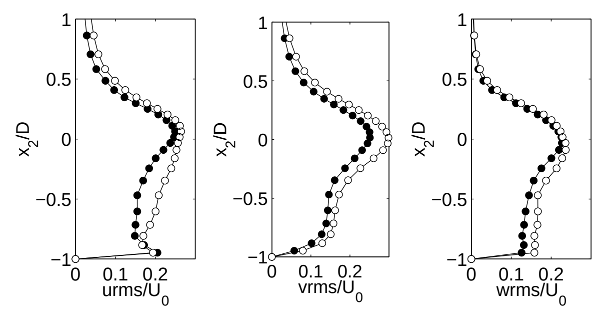

Figure 16: Comparison of *rms* velocity profiles at the location $x_1 = 2L/3$ for the 3Dr3T (-•-) and 3Dr3L (-○-) simulations.

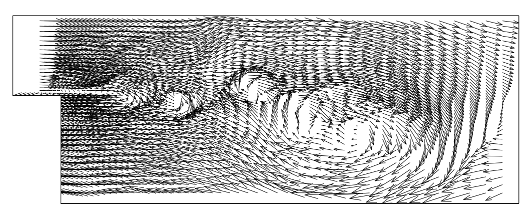

Figure 17: Zoom of velocity field around the upstream corner of the cavity for the turbulent simulation.

drop in passage frequency and a high spreading rate for the shear layer.

5.4 Acoustic field

The acoustic spectra for the turbulent and laminar cases are depicted in figure 18, and the predominance of the Strouhal number St=0.75 is observed in both cases. The acoustic level is reduced by 5 dB in the initially turbulent simulation 3Dr3T. This trend is conform to Karamcheti's results.[13] The latter noted a slightly lower frequency St=0.68 for the turbulent upstream boundary layer, and the intermittency with a low-frequency component St=0.33, which are not reproduced in our simulations. This is certainly attributable to the narrower width of the cavity investigated in the present simulation. Moreover, the role of the turbulence model, incorporated solely in the initially turbulent simulation, can be questionned and requires further validations.

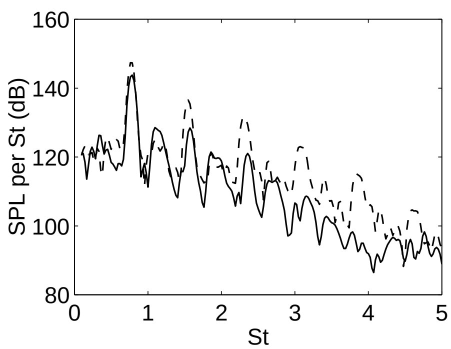

Figure 18: Spectra of pressure fluctuations at $x_1/D = -1.04$ and $x_2/D = 4.64$ versus the Strouhal number : (– – –), 3Dr3L run and (——), 3Dr3T run.

The pressure fields of figure 19 clearly illustrate the higher amplitude of the acoustic waves for the 3Dr3L simulation. The cross cuts show that sound waves are more two-dimensional in this case, whereas the fully turbulent cavity generates three-dimensional nonuniformities indicating a less coherent behaviour of the oscillations. The more coherent case leads to the appearance of important higher harmonics in the radiated field (see figure 18), as previously noted for the 3Dr1W simulation.

6. Conclusion

The principal observation in this study concerns the influence of the recirculating flow path modification on the self-excited oscillations within the cavity. In the 2-D simulations, it can lead to a wake mode régime, dominated by the ejection of a large recirculating eddy. For a highly three-dimensional case (3Dr1N run with $L/W > 1$), the oscillations are subject to jittering, e.g. irregularities in the vortex-impingement pattern. The comparison between runs 2Dr2TH with $L/\delta_\theta = 50$ and 3Dr1N with $L/\delta_\theta = 110$ shows that jitter becomes important for cavities with a longer impingement length

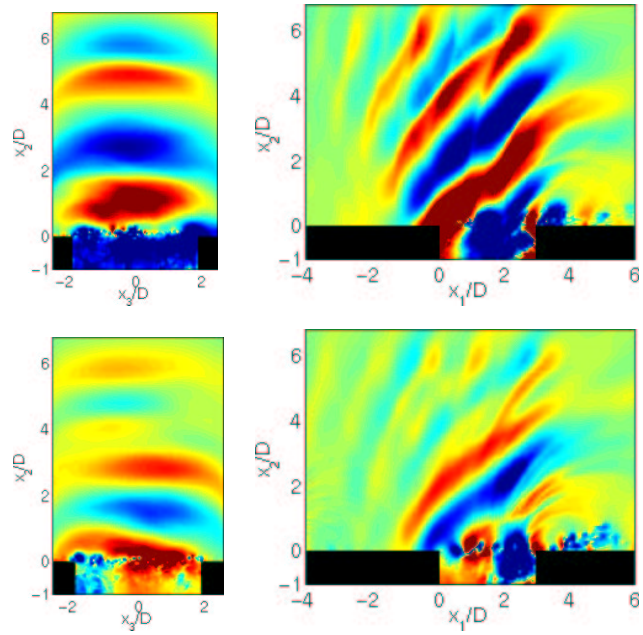

Figure 19: Pressure fields for the run 3Dr3L (top), and run 3Dr3T (bottom). Longitudinal views in the $x_3 = 0$ plane are presented on the right and cross views at $x_1 = 2.9D$ on the left. Levels between -3000 and 3000 Pa.

(relative to the shear layer thickness). This phenomenon tends to reduce the coherence of the self-sustained oscillations. Another effect which contributes to decrease the amplitude of the fluctuations is the turbulent state of the incoming boundary layer. These losses in coherence affect the strength of the upstream influence, and consequently the amplitude of the acoustic emission.

The strong unsteadiness of the recirculating flow can be associated to the possible vortex coalescence. It has often been said that the cavity shear layer does not present any vortex coalescence. This is not always true, and the 3Dr1W simulation show a quasi-two-dimensional pairing, although this fusion is less identifiable than vortex pairing in free mixing layers. The coalescence is now very deterministic and more diffuse in the whole process of shear layer growth. Another illustration is the fusion of two, three, four or more vortices after the upstream corner. This collective interaction depends on the level of forcing, and chiefly on the ratio L/δ_θ. Whether or not such coalescence occurs has important consequences for the frequency, scale, and vorticity concentrations of the vortices impinging on the downstream edge, as well as the magnitude of the resulting radiated noise.

Lastly, another important issue is the multiple frequency content of the spectra in the 3Dr1N and 3Dr1W simulations, with frequencies both higher and lower than the fundamental oscillation frequency. Vortex coalescence and wave selection associated with the finite cavity length can give rise to these various components. Nonlinear distorsions of the fundamental produce strong harmonics in the acoustic spectra of highly organized cavity flows. The absence of other modes in the 2Dr2TH run is linked to the relatively thick incoming boundary layer rather than to the bidimensional approach. Its stiffness precludes substantial modulations and leads to a single dominant mode. On the contrary, 3-D simulations with a thin incident boundary layer are sensitive to jittering effect by the recirculation and show a multiple frequency content.

Acknowledgments

Supercomputer time is supplied by Institut du Développement et des Ressources en Informatique Scientifique (IDRIS - CNRS).

References

[1] Rossiter, J.E. Wind-tunnel experiments on the flow over rectangular cavities at subsonic and transonic speeds. Technical Report 3438, *Aeronautical Research Council Reports and Memoranda*, 1964.

[2] Rockwell, D. & Knisely, C., 1980, Observations of the three-dimensional nature of instable flow past a cavity, *Phys. Fluids*, **23**(3), p. 425–431.

[3] Pereira, J.C.F. & Sousa, J.M.M., 1995, Experimental and numerical investigation of flow oscillations in a rectangular cavity, *ASME Journal of Fluids Engineering*, **117**, p. 68–74.

[4] Maull, D.J. & East, L.F., 1963, Three-dimensional flow in cavities, *J. Fluid Mech.*, **16**, p. 620–632.

[5] Kistler, A.C. & Tan, F.C., 1967, Some properties of turbulent separated flows, *The Physics of Fluids Supplement* Boundary Layers and Turbulence, p. S165–173.

[6] Chiang, T.P. & Sheu, W.H., 1997, Numerical prediction of eddy structure in a shear-driven cavity, *Computational Mechanics*, **20**, p. 379–396.

[7] Kuo, C.-H. & Huang, S.H., 2001, Influence of flow path modification on oscillation of cavity shear layer, *Experiments in Fluids*, **31**, p. 162–178.

[8] Knisely, C. & Rockwell, D., 1982, Self-sustained low frequency components in an impinging shear layer, *J. Fluid Mech.*, **116**, p. 157–186.

[9] Bogey, C. & Bailly, C., 2002, A family of low dispersive and low dissipative explicit schemes for computing aerodynamic, *AIAA Paper 2002-2509*.

[10] Bogey, C. & Bailly, C., 2002, Three-dimensional non-reflective boundary conditions for acoustic simulations : far field formulation and validation test cases, *Acta Acustica*, **88**, p. 463–471.

[11] Bailly, C., Lafon, P. & Candel, S., 1995, A stochastic approach to compute noise generation and radiation of free turbulent flows, *AIAA Paper 95-092*.

[12] Spalart, P.R., 1988, Direct simulation of a turbulent boundary layer up to $\mathrm{Re}_\theta = 1410$, *J. Fluid Mech.*, **187**, p. 61–98.

[13] Karamcheti, K. Acoustic radiation from two-dimensional rectangular cutouts in aerodynamic surfaces. *Tech. Note* 3487, NACA, 1955.

[14] Sarohia, V., 1977, Experimental oscillations in flows over shallow cavities, *AIAA Journal*, **15**(7), p. 984–991.

[15] Oster, D. & Wygnanski, I., 1982, The forced mixing layer between parallel streams, *J. Fluid Mech.*, **123**, p. 91–130.

[16] Forestier, N. *Etude expérimentale d'une couche cisaillée au-dessus d'une cavité en régime transonique.* PhD thesis, Ecole Centrale de Lyon, 2001. No NT 2001-1.

[17] Gloerfelt, X., Bailly, C. & Juvé, D., 2001, Computation of the noise radiated by a subsonic cavity using direct simulation and acoustic analogy, *AIAA Paper 2001-2226*.

[18] Rowley, C.W., Colonius, T. & Basu, A.J., 2002, On self-sustained oscillations in two-dimensional compressible flow over rectangular cavities, *J. Fluid Mech.*, **455**, p. 315–346.

[19] Shieh, C.M. *Parallel numerical simulations of subsonic, turbulent, flow-induced noise from two- and three-dimensional cavities using computational aeroacoustics.* PhD thesis, Pennsylvania State University, 2000.

[20] Comte, P., Silvestrini, J.H. & Bégou, P., 1998, Streamwise vortices in Large-Eddy simulations of mixing layers, *Eur. J. Mech. B/Fluids*, **17**(4), p. 615–637.

[21] Chandrsuda, C., Mehta, R.D., Weir, A.D. & Bradshaw, P., 1978, Effect of free-stream turbulence on large structure in turbulent mixing layers, *J. Fluid Mech.*, **85**(4), p. 693–704.

[22] Rockwell, D. & Knisely, C., 1980, Vortex-edge interaction: Mechanisms for generating low frequency components, *Phys. Fluids*, **23**(2), p. 239–240.

[23] Mendoza, J. & Ahuja, K.K., 1995, The effects of width on cavity noise, *AIAA Paper 95-054*.

[24] DeMetz, F.C. & Farabee, T.M., 1977, Laminar and turbulent shear flow induced cavity resonance, *AIAA Paper 77-1293*.

[25] Lin, J.C. & Rockwell, D., 2001, Organized oscillations of initially turbulent flow past a cavity, *AIAA Journal*, **39**(6), p. 1139–1151.

[26] Bernal, L.P. & Roshko, A., 1986, Streamwise vortex structure in plane mixing layers, *J. Fluid Mech.*, **170**, p. 499–525.

[27] Ho, C.-M. & Nosseir, N.S., 1981, Dynamics of an impinging jet. Part 1. The feedback phenomenon, *J. Fluid Mech.*, **105**, p. 119–142.